INTERNATIONAL JOURNAL FOR NUMERICAL METHODS IN FLUIDS
Int. J. Numer. Meth. Fluids 2006; **51**:1297–1318
Published online 20 December 2005 in Wiley InterScience (www.interscience.wiley.com). DOI: 10.1002/fld.1154

The Parabolic Spline Method (PSM) for conservative transport problems

M. Zerroukat*,†, N. Wood‡ and A. Staniforth§

Met Office, FitzRoy Road, Exeter EX1 3PB, U.K.

SUMMARY

A new and efficient parabolic spline based remapping algorithm is developed and tested herein. To ensure mass conservation, the scheme solves an integral form of the transport equation rather than the differential form. The integrals are computed from reconstructed parabolic splines with mass conservation constraints. For higher dimensions, this remapping can be used within a standard directional splitting methodology or within the flow-dependent cascade splitting approach. A grid and sub-grid based monotonic filter is also incorporated into the overall scheme. A truncation error analysis of the scheme is presented and discussed in terms of results from test cases. The analysis shows that although it has a similar truncation error in the converged limit as that of the widely used Piecewise Parabolic Method (PPM) for infinitely differentiable functions, PSM is more accurate than PPM for problems with slow spectral decay. Additionally, an operation count of the scheme is given which demonstrates the computational advantage of PSM compared to PPM. © Crown copyright 2005. Reproduced with the permission of Her Majesty's Stationery Office. Published by John Wiley & Sons, Ltd.

KEY WORDS: advection; conservation; monotonicity; PPM; remapping

1. INTRODUCTION

Remapping algorithms, such as the widely used Piecewise Parabolic Method (PPM) [1], are an important component in many advection schemes for conservative transport. These remappings are also the building blocks of many of the inherently conserving semi-Lagrangian schemes [2–11].

Herein, a more efficient variant of PPM based on the Parabolic Spline Method (PSM) is presented. PSM is similar to PPM but with additional smoothness arising from its 'best approximation' property. Truncation error analysis of both schemes shows that although both PPM and PSM have similar accuracy in the converged limit for infinitely differentiable

*Correspondence to: M. Zerroukat, Met Office, FitzRoy Road, Exeter EX1 3PB, U.K.
†E-mail: mohamed.zerroukat@metoffice.gov.uk
‡E-mail: nigel.wood@metoffice.gov.uk
§E-mail: andrew.staniforth@metoffice.gov.uk

Received 1 August 2005
Revised 28 October 2005
Accepted 7 November 2005

waves, PSM is more accurate than PPM for problems with slow spectral decay such as those occurring in atmospheric flow. Furthermore, an improved version of the monotonicity filter reported in Reference [12] is incorporated into the scheme. The filter achieves monotonicity without (except in extreme cases) reducing the order of the piecewise polynomial and hence it captures more accurately steep gradients (or curvature) without an artificial steepening approach.

The rest of the paper is organized as follows: Section 2 details the 1D remapping algorithm; in Section 3 the performance of the proposed scheme, and its comparison with PPM, is analysed using an operation count, truncation error analysis and numerical convergence tests; results using the proposed scheme with its monotonic filter are presented in Section 4 and compared with those using PPM and its monotonic filter; and conclusions are summarized in Section 5.

2. 1D REMAPPING

2.1. Problem definition

Consider passive 1D conservative transport of a scalar quantity ρ governed, in the absence of sources and sinks, by

$$\frac{\partial \rho}{\partial t} + \frac{\partial}{\partial x}(u\rho) = 0 \tag{1}$$

where $\rho(x,t)$ is the density (amount of scalar per unit length) of the transported quantity, and $u(x,t)$ is the transporting velocity field.

Integrating (1) with respect to x between two arbitrary moving boundaries $x_1 = x_1(x,t)$ and $x_2 = x_2(x,t)$, and making use of Leibniz' rule, leads to [5]

$$\frac{\mathrm{d}}{\mathrm{d}t}\int_{x_1(x,t)}^{x_2(x,t)} \rho \,\mathrm{d}x - \left[\rho(x_2,t)\frac{\mathrm{d}x_2}{\mathrm{d}t} - \rho(x_1,t)\frac{\mathrm{d}x_1}{\mathrm{d}t}\right] + [\rho(x_2,t)u(x_2,t) - \rho(x_1,t)u(x_1,t)] = 0 \tag{2}$$

If the boundaries x_1 and x_2 are moving with the fluid, i.e. if

$$\frac{\mathrm{d}x_1}{\mathrm{d}t} = u(x_1,t), \quad \frac{\mathrm{d}x_2}{\mathrm{d}t} = u(x_2,t) \tag{3}$$

then (2) simplifies to the classical integral form of the tracer conservation equation

$$\frac{\mathrm{d}M(x_1,x_2,t)}{\mathrm{d}t} \equiv \frac{\mathrm{d}}{\mathrm{d}t}\left(\int_{x_1(t)}^{x_2(t)} \rho(x,t)\,\mathrm{d}x\right) = 0 \tag{4}$$

Equation (4) simply states that the mass $M(x_1,x_2,t)$ contained between any two boundaries $x_1(t)$ and $x_2(t)$, moving with the fluid, is invariant in time, i.e. M is conserved.

Since $x_1(t)$ and $x_2(t)$ in (4) are any two points travelling with the fluid, one can consider that these moving boundaries instantaneously coincide at time t^{n+1} with the boundaries of an Eulerian Control Volume (ECV), whilst their upstream positions $x_1(t^n)$ and $x_2(t^n)$ at time t^n form the left and right boundaries of the associated upstream Lagrangian Control

Volume (LCV). In other words, since the fluid is a continuum, then the fluid contained in the Lagrangian segment $[x_1^d, x_2^d] \equiv [x_1(t^n), x_2(t^n)]$ is completely transported to the Eulerian segment $[x_1(t^{n+1}), x_2(t^{n+1})]$ (this provides the basis of the SLICE scheme [2]).

To discretize (4), consider the general case where the computational 1D domain $\Omega = [x_{\min}, x_{\max}]$ is subdivided into N ECVs with (possibly unequal) spacing $h_i \equiv x_{i+1/2} - x_{i-1/2}$ $(i = 1, 2, \ldots, N)$, where $x_{i-1/2}$ and $x_{i+1/2}$ are, respectively, the left and right boundaries of ECV_i.

Defining the gridbox-averaged density at time t as

$$\bar{\rho}_i(t) \equiv \frac{1}{h_i} \int_{x_{i-1/2}}^{x_{i+1/2}} \rho(x,t)\,\mathrm{d}x \equiv \frac{1}{h_i} M(x_{i-1/2}, x_{i+1/2}, t) \equiv \frac{1}{h_i} M_i \tag{5}$$

the time-discretization of (4) can then be rewritten as

$$\bar{\rho}_i^{n+1} \equiv \bar{\rho}_i(t^{n+1}) \equiv \frac{1}{h_i}(M_i)^{n+1} = \frac{1}{h_i}(M_i^d)^n \tag{6}$$

where

$$M_i^d \equiv \int_{x_{i-1/2}^d}^{x_{i+1/2}^d} \rho(x,t)\,\mathrm{d}x \tag{7}$$

Here superscript n denotes evaluation at time t^n, superscript d denotes association with a departure-point value (as in semi-Lagrangian schemes [13]), and $x_{i-1/2}^d$ and $x_{i+1/2}^d$ are, respectively, the left- and right-hand boundaries of LCV_i at time t^n, determined from numerical integration of (3)—see, e.g. Reference [13].

In general, the shape of $\rho(x, t^n)$ is not known *a priori*. Instead piecewise polynomials that use the given discrete gridbox-averaged values can be reconstructed. Previous approaches have used either piecewise constant, piecewise linear [14], piecewise parabolic [1, 5] or piecewise cubic [2, 8] polynomials. Herein a parabolic spline method is proposed.

2.2. *The parabolic spline method* (*PSM*)

2.2.1. Formulation. Let $\rho_i(x)$ be a local (i.e. specific to ECV_i) parabola defined on the interval $[x_{i-1/2}, x_{i+1/2}]$. $\rho_i(x)$ may be uniquely defined in terms of the two meshpoint values $\rho_{i-1/2} \equiv \rho_i(x_{i-1/2})$, $\rho_{i+1/2} \equiv \rho_i(x_{i+1/2})$ and the interval-averaged value

$$\bar{\rho}_i \equiv \frac{1}{h_i} \int_{x_{i-1/2}}^{x_{i+1/2}} \rho_i(x)\,\mathrm{d}x \tag{8}$$

Thus

$$\rho_i(\xi) = a_i^{(0)} + a_i^{(1)}\xi + a_i^{(2)}\xi^2, \quad \xi \in [0,1] \tag{9}$$

where $\xi \equiv (x - x_{i-1/2})/h_i$ is a dimensionless local coordinate, and $(a_i^{(0)}, a_i^{(1)}, a_i^{(2)})$ are coefficients defined such that

$$a_i^{(0)} = \rho_{i-1/2} \tag{10}$$

$$a_i^{(1)} = -4\rho_{i-1/2} - 2\rho_{i+1/2} + 6\bar{\rho}_i \tag{11}$$

$$a_i^{(2)} = 3\rho_{i-1/2} + 3\rho_{i+1/2} - 6\bar{\rho}_i \tag{12}$$

$$\bar{\rho}_i = \int_0^1 \rho_i(\xi)\,\mathrm{d}\xi \tag{13}$$

By construction $\rho_i(x)$, as a piecewise parabola defined by (9) for $i = 1, 2, \ldots$, is continuous at all meshpoints $x_{i\pm1/2}$, $i = 1, 2, \ldots$. However, only the interval averaged quantities $\bar{\rho}_i$ are known, the meshpoint values $\rho_{i+1/2}$ are not. The problem is closed and $\rho_{i+1/2}$ determined by imposing the condition that its first derivative also be continuous at these same meshpoints. This condition defines a parabolic spline, and yields an equation that relates the three quantities $\rho_{i-1/2}$, $\rho_{i+1/2}$ and $\rho_{i+3/2}$ to $\bar{\rho}_i$ and $\bar{\rho}_{i+1}$. This is achieved by making use of (10)–(12) and equating $(\mathrm{d}\rho_i/\mathrm{d}x)|_{x_{i+1/2}}$ and $(\mathrm{d}\rho_{i+1}/\mathrm{d}x)|_{x_{i+1/2}}$, which gives

$$\frac{1}{h_i}\rho_{i-1/2} + 2\left(\frac{1}{h_i} + \frac{1}{h_{i+1}}\right)\rho_{i+1/2} + \frac{1}{h_{i+1}}\rho_{i+3/2} = 3\left(\frac{1}{h_i}\bar{\rho}_i + \frac{1}{h_{i+1}}\bar{\rho}_{i+1}\right) \tag{14}$$

It is the fact that the given quantities are the *interval-averaged values* $\bar{\rho}_i$ rather than the *meshpoint values* $\rho_{i+1/2}$ that makes the problem here different to the definition of a traditional spline. Equation (14) defines a linear system of equations for the unknown ρ's in terms of the known $\bar{\rho}$'s. Boundary conditions are required to close the problem and this is achieved in an analogous manner to that used to define a traditional cubic spline (e.g. see References [15, 16] and also Section 2.2.2 below). For a bounded domain, the simplest way of determining the two missing degrees of freedom is to impose $\mathrm{d}\rho/\mathrm{d}x = 0$ at the two endpoints $x = x_{1/2}$ and $x = x_{N+1/2}$, corresponding to an assumption of zero slope there. These are the natural conditions for the parabolic spline defined here, see Section 2.2.2 for details. Other choices are also possible—see e.g. References [15, 16]. For a periodic domain, the problem is closed via the application of periodicity.

The matrix associated with the system of linear equations defined by (14) and associated boundary conditions is tridiagonal with non-zero determinant and is invertible. Solving this system for the ρ's results in all the coefficients of all the parabolae $\rho_i(\xi)$, $i = 1, 2, \ldots, N$, defined by (9), being known. The reconstructed function then constitutes a parabolic spline since it is piecewise parabolic and is everywhere continuous with continuous first derivatives, including at the interval boundaries (also known as knots).

2.2.2. Link with classical cubic splines and best approximation. To link the parabolic spline developed above to classical cubic splines, first define a new variable, cumulative mass, by

$$R(x) \equiv R_{1/2} + \int_{x_{1/2}}^{x} \rho(x)\,\mathrm{d}x \tag{15}$$

where $R_{1/2}$ is a constant. Differentiating (15) gives

$$\frac{\mathrm{d}R(x)}{\mathrm{d}x} = \rho(x) \tag{16}$$

which, after integration from $x = x_{i-1/2}$ to $x = x_{i+1/2}$ and use of (8), then yields

$$\frac{1}{h_i}(R_{i+1/2} - R_{i-1/2}) = \frac{1}{h_i}\int_{x_{i-1/2}}^{x_{i+1/2}} \rho(x)\,\mathrm{d}x \equiv \bar{\rho}_i \tag{17}$$

Equation (14) can now be rewritten using (17) as

$$\frac{1}{h_i}\rho_{i-1/2}+2\left(\frac{1}{h_i}+\frac{1}{h_{i+1}}\right)\rho_{i+1/2}+\frac{1}{h_{i+1}}\rho_{i+3/2}=\frac{3}{h_i^2}(R_{i+1/2}-R_{i-1/2})+\frac{3}{h_{i+1}^2}(R_{i+3/2}-R_{i+1/2}) \qquad (18)$$

Comparing this with (2.1.14) of Reference [15], and taking account of differences in notation ($\rho \to m, R \to y$) and indexing convention (all indices of ρ and R are decremented by $1/2$), it is seen that they are formally equivalent. Thus the parabolic spline defined herein in terms of the discrete values $\bar{\rho}_i$ can be considered to be equivalent to a classical cubic spline defined in terms of the discrete values $R_{i+1/2}$ of a cumulative mass function. In other words the values of $\rho_{i+1/2}$ obtained from (14) are the same as would result from fitting a classical cubic spline through the discrete values $R_{i+1/2}$ of the cumulative mass function (15). These latter, if needed, can be recursively materialized from (15) by imposing the arbitrary reference value $R_{1/2}=0$ (the $R_{i+1/2}$'s are only defined to within an arbitrary additive constant).

A property of classical cubic splines (Section 2.2 in Reference [15]) is the 'best approximation' property: of all piecewise-cubic functions, the cubic spline is optimal in the sense that it minimizes the integrated square curvature, and it is therefore the smoothest such function to fit given data. In the present context, this means that the parabolic spline defined herein can be viewed as having a 'best approximation' property for the representation of the cumulative mass function R.

From (16), $\mathrm{d}^2R/\mathrm{d}x^2=\mathrm{d}\rho/\mathrm{d}x$. Thus minimizing the integrated squared curvature of R over the domain, i.e. minimizing $I\equiv\sum_i\int_{x_{i-1/2}}^{x_{i+1/2}}(\mathrm{d}^2R/\mathrm{d}x^2)^2\,\mathrm{d}x$, is equivalent to minimizing $I=\sum_i\int_{x_{i-1/2}}^{x_{i+1/2}}(\mathrm{d}\rho_i/\mathrm{d}x)^2\,\mathrm{d}x$. It can be verified that this is indeed true for the parabolic spline defined herein. First note that

$$I\equiv\sum_i\int_{x_{i-1/2}}^{x_{i+1/2}}\left[\frac{\mathrm{d}\rho_i(x)}{\mathrm{d}x}\right]^2\mathrm{d}x=\sum_i\frac{1}{h_i}\int_0^1\left[\frac{\mathrm{d}\rho_i(\xi)}{\mathrm{d}\xi}\right]^2\mathrm{d}\xi=\sum_i\frac{1}{h_i}\int_0^1[a_i^{(1)}+2a_i^{(2)}\xi]^2\,\mathrm{d}\xi \qquad (19)$$

For a periodic domain, explicit substitution of (11) and (12) into (19), followed by minimization with respect to the coefficients $\rho_{i-1/2}$, then leads to (14) which (after the periodic 'wrap-around') holds at all points in the domain. It is the key condition that turns the piecewise-parabolic function into a parabolic spline. For a bounded domain, applying the same procedure for the coefficients $\rho_{3/2},\rho_{5/2},\ldots,\rho_{N-1/2}$ also leads to (14). Applying this procedure for $\rho_{1/2}$ and $\rho_{N+1/2}$ leads to $(2\rho_{1/2}+\rho_{3/2}-3\bar{\rho}_1)=0$ and $(\rho_{N-1/2}+2\rho_{N+1/2}-3\bar{\rho}_N)=0$, respectively. These are exactly the results that are obtained if the definition of the parabolic spline is closed by imposing the boundary condition $\mathrm{d}\rho/\mathrm{d}x=0$ at the endpoints $x_{1/2}$ and $x_{N+1/2}$. From (16), when constructing a cubic spline in terms of the cumulative mass function R, this corresponds to imposing $\mathrm{d}^2R/\mathrm{d}x^2=0$ at the boundaries. This is the 'natural' boundary condition for a cubic spline [15], so $\mathrm{d}\rho/\mathrm{d}x=0$ can be viewed as being the 'natural' boundary condition for the equivalent parabolic spline defined herein.

2.2.3. Monotonicity. Having determined the properties of each local parabola, a monotonicity filter is used to detect spurious non-monotonic behaviour at the grid and sub-grid scales, and to then modify locally the parabola to restore monotonicity. This is achieved using an improved version of the algorithm detailed in Reference [12]. The algorithm has two parts: (i) detection of Control Volumes (CVs) where monotonicity is spuriously violated; and

(ii) for these flagged CVs, successive local reduction of the degree or reduction in continuity of the piecewise polynomial representation until monotonicity is achieved.

There are two possible sources for the spurious violation of monotonicity which can be characterized as being grid-scale and sub-grid-scale. Firstly, the estimates $\{\rho_{i-1/2}, i=1,\ldots,N+1\}$ at the CV boundary of each parabola, as a complete set, are tested for undershoots and overshoots with respect to $\{\bar{\rho}_i, i=1,\ldots,N\}$. This is termed grid-scale violation and the algorithm in Reference [12] is used to identify and modify the set $\{\rho_{i-1/2}, i=1,\ldots,N+1\}$ accordingly. Secondly, the local parabola may itself spuriously violate monotonicity within the interval over which it is defined. This is a sub-grid-scale violation. In the present algorithm it is this sub-grid violation which is treated differently from the approach in Reference [12].

Assume that an interval has been detected that is not monotonic. The underlying strategy adopted in Reference [12] for imposing monotonicity is: (i) to always retain the conservation constraint (13); (ii) to progressively degrade the order of the reconstruction polynomial by introducing local discontinuities; while (iii) to the extent possible, trying to respect one of the two left-interval and right-interval values. In this paper, step (ii) is slightly modified so that the order of the reconstruction is maintained if possible, albeit at the expense of continuity. This improved approach of achieving monotonicity while maintaining a higher degree polynomial, allows the filter to better capture steep gradients in regions of undershoots and overshoots. This results in better accuracy and less damping for such regions. Using the nomenclature in Reference [1], this can be seen as 'steepening', albeit not artificial but rather an approximation to the true steepness (or curvature). Therefore, if the original parabola is found to be not monotonic, instead of fitting a linear profile, the new approach consists of fitting a monotone parabola but one which does not maintain continuity at both edges of the interval (as indeed is generally the case when a linear profile is used directly).

The parabola (9) is judged to be monotone if it is strictly increasing or strictly decreasing in the interval $0 \leqslant \xi \leqslant 1$. It can still be judged not to violate monotonicity even when there is a local (i.e. $\xi \in [0,1]$) extremum, provided that this extremum is judged to be genuine. Authenticity of a local extremum is determined by examining the distribution of $\rho_{i-1/2}$ in the neighbouring CVs—see Reference [12] for details.

Consider the case of a CV_i with $\rho_{i+1/2} > \rho_{i-1/2}$ (similar equations apply when $\rho_{i+1/2} < \rho_{i-1/2}$), then the piecewise parabola (9) is not monotone within the interval $[0,1]$ (i.e. it has an extremum outside the range $[\rho_{i-1/2}, \rho_{i+1/2}]$) if

$$\bar{\rho}_i < \rho_i^l \equiv \tfrac{2}{3}\,\rho_{i-1/2} + \tfrac{1}{3}\,\rho_{i+1/2} \tag{20}$$

or

$$\bar{\rho}_i > \rho_i^u \equiv \tfrac{1}{3}\,\rho_{i-1/2} + \tfrac{2}{3}\,\rho_{i+1/2} \tag{21}$$

It can be argued that in these cases (i.e. when (20) or (21) hold), which can be considered as cases of 'steep gradient', a linear polynomial reconstruction cannot be considered as a good approximation, and a higher-order polynomial is needed to better approximate the curvature. Therefore, the new approach is to replace the original parabolic spline by a locally defined parabola which has the properties: (i) it preserves the local density average value; (ii) it passes through at least one boundary value ($\rho_{i-1/2}$ or $\rho_{i+1/2}$); and (iii) it is locally monotonic in the interval $[0,1]$. The monotonic constraint (iii) can be achieved by requiring zero derivative (the limiting case of the original parabola being monotone) at the boundary ($\xi = 0$ or $\xi = 1$)

identified at step (ii). The coefficients of these parabolae for the case of $\rho_{i+1/2} > \rho_{i-1/2}$ are given by

$$\begin{aligned} (a_i^{(0)}, a_i^{(1)}, a_i^{(2)}) &= (\rho_{i-1/2}, 0, -3\rho_{i-1/2} + 3\bar{\rho}_i) && \text{if } \bar{\rho}_i < \rho_i^l \\ (a_i^{(0)}, a_i^{(1)}, a_i^{(2)}) &= (-2\rho_{i+1/2} + 3\bar{\rho}_i, 6\rho_{i+1/2} - 6\bar{\rho}_i, -3\rho_{i+1/2} + 3\bar{\rho}_i) && \text{if } \bar{\rho}_i > \rho_i^u \end{aligned} \tag{22}$$

Note that the first parabola in (22) satisfies (13), $\rho_i(\xi = 0) = \rho_{i-1/2}$, $\mathrm{d}\rho_i/\mathrm{d}\xi|_{\xi=0} = 0$ and $\rho_i(\xi = 1) < \rho_{i+1/2}$, whereas the second one in (22) satisfies (13), $\rho_i(\xi = 1) = \rho_{i+1/2}$, $\mathrm{d}\rho_i/\mathrm{d}\xi|_{\xi=1} = 0$ and $\rho_i(\xi = 0) > \rho_{i-1/2}$. Viewing the problem as one of constrained optimization, it can be shown that this locally defined parabola (22) is optimal in that it minimizes the integrated square difference, over the interval $0 \leqslant \xi \leqslant 1$, between itself and the original parabolic spline subject to the requirements of monotonicity. When $\rho_i^l \leqslant \bar{\rho}_i \leqslant \rho_i^u$ the original parabola is monotone and no modification is required. If $\bar{\rho}_i$ is outside the range $[\rho_{i-1/2}, \rho_{i+1/2}]$, then no higher-degree (greater than zero) reconstruction satisfies monotonicity and the use of a piecewise constant reconstruction is the only choice left, i.e.

$$(a_i^{(0)}, a_i^{(1)}, a_i^{(2)}) = (\bar{\rho}_i, 0, 0) \quad \text{if } (\bar{\rho}_i - \rho_{i-1/2})(\bar{\rho}_i - \rho_{i+1/2}) \leqslant 0 \tag{23}$$

It is worth mentioning that in this modified filter the use of a linear reconstruction becomes obsolete except for the natural case of $\bar{\rho}_i = (\rho_{i-1/2} + \rho_{i+1/2})/2$ where the original parabola degenerates to a straight line.

2.3. Computation of piecewise integrals

Having defined the piecewise $\rho_i(x)$ for each ECV_i, the mass $(M_i^d)^n$, given by (7), of LCV_i, which extends over the segment $[x_{i-1/2}^d, x_{i+1/2}^d]$ at time t^n, is computed as

$$(M_i^d)^n = \begin{cases} h_l \displaystyle\int_{\xi_{i-1/2}^d}^{1} \rho_l^n(\xi)\,\mathrm{d}\xi + \sum_{j=l+1}^{m-1} h_j \bar{\rho}_j^n + h_m \int_0^{\xi_{i+1/2}^d} \rho_m^n(\xi)\,\mathrm{d}\xi, & m \geqslant l+1 \\ h_l \displaystyle\int_{\xi_{i-1/2}^d}^{\xi_{i+1/2}^d} \rho_l^n(\xi)\,\mathrm{d}\xi, & m = l \end{cases} \tag{24}$$

where l and $m \geqslant l$ are the ECV indices associated with the segments in which $x_{i-1/2}^d$ and $x_{i+1/2}^d$ lie, i.e. $x_{i-1/2}^d \in [x_{l-1/2}, x_{l+1/2}]$ and $x_{i+1/2}^d \in [x_{m-1/2}, x_{m+1/2}]$. Also $\xi_{i\pm1/2}^d$ are the local coordinates corresponding to $x_{i\pm1/2}^d$, i.e. $\xi_{i-1/2}^d = (x_{i-1/2}^d - x_{l-1/2})/h_l$ and $\xi_{i+1}^d = (x_{i+1/2}^d - x_{m-1/2})/h_m$. The integrals on the right-hand side of (24) are evaluated analytically.

For higher dimensions, the present 1D remapping algorithm can be used within a standard directional splitting methodology or within the flow-dependent cascade methodology used in SLICE [2, 3]. In both approaches, a 2D (or 3D) problem is spatially split into sets of 1D remapping problems to be solved using an algorithm such as PSM or PPM. The directional splitting strategy (e.g. Reference [17] using PPM) decomposes a multi-dimensional problem into sets of 1D problems aligned in fixed directions parallel to the coordinate axes. A drawback however is that it leads to significant truncation errors which can unduly limit the timestep for accuracy reasons [18]. To address this issue, the flow-dependent cascade strategy adopts a different decomposition. A set of 1D remappings, aligned with one of the coordinate

axes, is first performed as in the directional splitting method. However, the second set (and third for 3D problems) of 1D remappings is instead performed in directions aligned not with a fixed time-independent coordinate axis, but with that of a flow-dependent Lagrangian mesh that evolves in time. Details, together with results in both Cartesian and spherical geometries, may be found in Reference [19].

3. OPERATION COUNTS AND TRUNCATION ERRORS FOR PSM AND PPM

3.1. Operation counts

Appendix A details the operation count for a 1D algorithm based on PSM or PPM. It is found that for a non-uniform, dynamically varying grid, where pre-computation of grid-based quantities is not possible, PPM is about 60% more expensive than PSM.

3.2. Truncation error analysis

The analysis of the truncation error for a non-uniform grid (i.e. $h_i \neq h_{i+1}$) shows that both PSM and PPM are third-order accurate in space, while for a uniform grid ($h_i = h$) they are both fourth-order accurate, see details in Appendix B. The results also show that for a uniform grid, the leading error terms are the same for the asymptotic (converged) regime ($h \to 0$). However, the leading terms for a non-uniform grid are different but for a smoothly varying grid the difference between the two terms is negligible, except for unrealistically large stretching of the grid ($h_i/h_{i+1} \gg 1$ or $h_i/h_{i+1} \ll 1$). In what follows these results are confirmed empirically from convergence tests applied to uniform advection of a sine wave.

3.2.1. Convergence for uniform advection of a sine wave. Let the computational domain be an interval $\Omega \equiv \{x \in [0, 2L] \equiv [x_{1/2}, x_{N+1/2}]\}$ divided into N sub-intervals $h_i \equiv x_{i+1/2} - x_{i-1/2}$, $i = 1, \ldots, N$. Given an initial value problem with an average density distribution $(\bar{\rho}_1, \ldots, \bar{\rho}_N)$ and an advection velocity $u(x, t)$, then the problem is to compute, using the 1D remapping algorithm of Section 2, the discrete solution $\{\bar{\rho}_1^{n+1}, \ldots, \bar{\rho}_N^{n+1}\}$ at time $t^{n+1} \equiv t^n + \Delta t$ from the known solution $\{\bar{\rho}_1^n, \ldots, \bar{\rho}_N^n\}$ at time t^n. The first test is for uniform advection of a sine wave, where the initial distribution is

$$\bar{\rho}(x, 0) = \sin\left(\frac{\pi x}{L}\right) \tag{25}$$

and $u(x, t) = U = 1$.

Table I displays the convergence of l_2 error (see Appendix C for its definition) for this test, as a function of resolution N, when using PSM and PPM on a uniform grid (parameters as specified in the table and $h_i = h$). It can be seen that at lower resolutions PSM has a smaller error than PPM, but in the asymptotic regime they have similar errors (i.e. the ratio of the two errors, r, tends to 1 as N increases). It can also be verified using the data in Table I that the order of convergence is 4 (i.e. $|\bar{\rho}^{\text{num}} - \bar{\rho}^{\text{an}}| \propto h^4$) for both PPM and PSM. Similar results, not shown, for a smoothly varying (non-uniform) grid show that, as expected, the order of convergence of both PPM and PSM is 3 and $r \to 1$ as N increases. These results are in agreement with the truncation error analysis of Appendix B.

Table I. Convergence of l_2 error as a function of resolution N (= number of intervals) for uniform advection of a sine wave on a periodic domain with $L = 1/2$, $\varepsilon = 0.12$ ($\varepsilon \equiv U\Delta t/h$ = Courant number) and 20 timesteps. The ratio r is defined as $r \equiv l_2(\text{PPM})/l_2(\text{PSM})$.

N	8	16	32	64	128	256	512
l_2(PPM)	0.174E−01	0.587E−03	0.220E−04	0.102E−05	0.565E−07	0.341E−08	0.211E−09
l_2(PSM)	0.549E−02	0.254E−03	0.143E−04	0.872E−06	0.541E−07	0.337E−08	0.211E−09
r	3.159	2.314	1.532	1.165	1.044	1.011	1.003

Table II. As in Table I but for uniform advection of an isolated cosine-squared hill with $l = 7/64$.

N	16	32	64	128	256	512
l_2(PPM)	0.340E+00	0.458E−01	0.489E−02	0.801E−03	0.139E−03	0.246E−04
l_2(PSM)	0.230E+00	0.262E−01	0.260E−02	0.440E−03	0.769E−04	0.136E−04
r	1.479	1.746	1.881	1.823	1.813	1.810

3.2.2. Convergence for uniform advection of a cosine-squared hill. Convergence is now examined for a slightly more practical problem, that of uniform advection of an isolated cosine-squared hill [6, 7, 9–12, 17, 20]. The initial distribution is

$$\bar{\rho}(x,0) = \begin{cases} \cos^2\left[\dfrac{\pi(x-L)}{2l}\right] & \text{for } L-l \leqslant x \leqslant L+l \\ 0 & \text{otherwise} \end{cases} \tag{26}$$

where $0 < l < L$, and it is again solved on the domain $x \in [0, 2L]$ with uniform velocity $u(x,t) = U = 1$.

Table II displays the convergence of l_2 error for this test, as a function of resolution N, when using PSM and PPM on a uniform grid with the same parameters as for the sine-wave problem above. It can be seen that the ratio of the error of PPM to that of PSM, r, does not converge to 1 as is the case for a pure sine wave and as would be expected from the truncation error analysis. The ratio r is maintained at 1.8 even for N as large as $N = 16\,284$. This indicates an advantage of PSM compared to PPM, even in the converged limit.

3.2.3. Convergence discussion. These two results (that the PPM and PSM errors converge asymptotically to each other for a sine wave but that PPM converges to a significantly larger error than PSM for the isolated cosine-squared hill) can be reconciled by noting that despite the cosine-squared hill being relatively smooth (it is continuous and has continuous first derivative everywhere), its second derivative is discontinuous at $x = L \pm l$ leading to a relatively slow spectral decay. The consequence of this slow spectral decay is discussed in the following.

For a given resolution, consider what range of wavenumbers (k) are well resolved, in the sense that the asymptotic truncation error is applicable (and therefore that the PSM and PPM results converge). This requires that, in the truncation error analysis, the higher order terms in kh should be negligibly small, i.e. $kh \ll 1$. Specifically (but somewhat arbitrarily), let this

requirement be that $kh \leqslant 1/10$. This requires the non-dimensional wavenumber k^* to satisfy

$$k^* \leqslant \frac{N}{20\pi} \tag{27}$$

where $k^* \equiv k(2L)/(2\pi)$ takes all integer values between 1 and $N/2$, and for uniform resolution $h \equiv (2L)/N$, N being the number of grid points. For the example presented in Table I, $k^* = 1$ and (27) then suggests that this wave will only be well resolved (and therefore that the PSM and PPM results will converge) for a resolution of at least 60 grid points. This is supported by the results of Table I.

Since $1 \leqslant k^* \leqslant N/2$, (27) implies that approximately only the lowest 1/30th of the spectrum is well resolved. For the remaining part (the majority) of the spectrum, the higher order terms in the truncation error analysis are likely to be important (thereby invalidating use of the expansion used in the truncation error analysis). Therefore, in order for the asymptotic truncation error to be applicable to any experimental comparison between PSM and PPM (and hence for the experimentally determined errors to converge) the spectrum of the shape being advected must decay rapidly as k^* increases, so that negligibly small power remains in those wavenumbers for which higher order terms in the truncation error analysis are significant.

The error associated with any given wavenumber, $\mathscr{E} = \mathscr{E}(k, h, \varepsilon, \bar{\rho}, N)$ (where ε is the Courant number and $\bar{\rho}$ is the shape being advected), is the product of the truncation error, $\mathscr{T}(kh, \varepsilon)$, and the spectral amplitude, $\mathscr{S}(k, \bar{\rho}, N)$. The total error of a scheme is given by the sum of $\mathscr{E}$ over all wavenumbers. Of interest is whether the spectral decay of any given shape is rapid enough for the total error to be dominated by the asymptotic truncation error, i.e. by the well resolved wavenumbers. A pragmatic estimate of whether this is the case can be obtained by considering only the well resolved end of the spectrum, $1 \leqslant k^* \leqslant N/(20\pi)$, and assuming that the asymptotic (large k^*) spectral decay of the shape is known. (For there to be a significant overlap between $1 \leqslant k^* \leqslant N/(20\pi)$ and $k^* \gg 1$ requires N to be large.) Then, for fixed resolution, $\mathscr{T}$ varies as k^p where p is the order of the scheme and $\mathscr{S}$ varies as k^{-q} where q is the asymptotic decay rate of the spectrum of the shape being advected. Therefore, the error varies as

$$\mathscr{E} \propto k^{p-q} \tag{28}$$

From this it is clear that, provided the assumptions of this approximate analysis hold, when $p < q$ the relative errors for different wavenumbers will increase as the wavenumber *decreases*. If this is so then the total error (integrated over the whole spectrum) is likely to be dominated by the error of the smaller wavenumbers for which the asymptotic truncation error is applicable. In contrast, when $p > q$, the error will increase as the wavenumber *increases* and the total error is likely to be dominated by the larger wavenumbers for which the higher order (in kh) contributions to the truncation error are likely to be important.

On a uniform grid, $p = 4$ for both PSM and PPM. For the cosine-squared hill, the (continuous) Fourier series spectral coefficients decay asymptotically as k^{-3} for large k so that $q = 3$. Therefore, $p > q$ and the comparison of errors between PPM and PSM is likely to be dominated, not by the asymptotic truncation error (which are the same for both PPM and PSM), but by the higher order terms which are different for PPM and PSM. In order for this not to be the case, and so to obtain the expected convergence of PPM to PSM, the spectrum of the data being reconstructed or advected, must decay faster than the truncation error so that $q > p$. This is demonstrated in Table III where the results of the same error ratio tests

Table III. Ratio $r \equiv l_2(\text{PPM})/l_2(\text{PSM})$ at different resolutions N for the generalized cosine hill (29) with different powers n. $L = 1/2$, $l = 7/64$, $\varepsilon = 0.12$ and 20 timesteps.

N	32	64	128	256	512	1024	2048
$n=2$	1.746	1.881	1.823	1.813	1.810	1.810	1.810
$n=3$	2.474	2.332	1.968	1.864	1.852	1.854	1.858
$n=4$	2.148	3.065	2.508	1.767	1.327	1.134	1.057
$n=5$	1.888	3.127	2.643	1.763	1.258	1.072	1.019

as for the cosine-squared hill are presented. Consider the following generalized cosine hill of order n, namely

$$\bar{\rho}(x,0) \equiv \begin{cases} \cos^n\left[\dfrac{\pi(x-L)}{2l}\right] & \text{for } L-l \leqslant x \leqslant L+l \\ 0 & \text{otherwise} \end{cases} \tag{29}$$

on the domain $[0, 2L]$ with n a positive integer and $0 < l < L$. This generalized cosine hill (29) is continuous, has its first $n-1$ derivatives continuous and its spectrum decays asymptotically as $k^{-(n+1)}$. Then since, on a uniform grid, PPM and PSM have $p = 4$, the total error is expected to be well approximated by the asymptotic truncation error when $n+1 > 4$, i.e. for $n > 3$. This is indeed what is observed in Table III. The case $n = 4$ is the first for which PPM asymptotically has the same error as PSM.

From an intuitive perspective it would seem that the cosine-squared hill is not that pathological, being relatively smooth. Indeed it is for this reason that it has been used for testing the behaviour of advection schemes [6, 7, 9–12, 17, 20]. Therefore, the above results raise important questions about the relevance of convergence tests (other than as important coding tests). But are the results of practical significance?

An example which suggests that they may indeed be so is numerical weather prediction (NWP). This is an important problem which presents a critical challenge to CFD and which is arguably dominated by advection. A crucial aspect of the atmosphere from an NWP perspective is the slow decay of the atmospheric energy spectrum. Nastrom and Gage [21] derived a climatology of the atmospheric energy spectrum over scales ranging from 3 to nearly 10 000 km (see also Reference [22] for further discussion of atmospheric spectra). For synoptic scales (10 000–2 000 km) the Nastrom-Gage energy spectrum decays as k^{-3} whilst for meso- and even smaller scales (around 600–3 km), the Nastrom-Gage energy spectrum decays more slowly as $k^{-5/3}$. This spectrum is itself distinct from the Kolmogorov $k^{-5/3}$ spectrum for homogeneous three-dimensional turbulence which arises at much smaller scales, with wavelengths significantly less than the height above the surface [23]. Noting that these spectral decay estimates are for energy spectra, it is to be expected that in all practical meteorological applications, the asymptotic truncation error is unlikely to be applicable to the comparison of the convergence of advection schemes.

4. MONOTONIC RESULTS

To test the monotonicity part of the algorithm, let the initial distribution be given by [12]

$$\bar{\rho}(x,0;C) = \{\tanh[c_1(x-c_2)] + \tanh[c_3(x-c_4)]\}\{1+c_5\sin(2\pi c_6 x)\}\{1+c_7\sin(2\pi c_8 x - c_9)\}$$
$$+ \{\tanh[c_{10}(x-c_{11})] + \tanh[-c_{10}(x-c_{12})]\} + c_{13} \tag{30}$$

where $C = \{c_1, \ldots, c_{13}\}$ is a set of constants. Two variants of this problem are used for evaluation purposes: an irregular signal with mixed smooth and unsmooth parts, including quasi-discontinuities, and a profile having steep gradients.

To simplify nomenclature within this section, 'PSM'/'PPM' signifies the use of PSM/PPM *without* their respective monotonicity filters activated: similarly for 'PSM-M'/'PPM-M' but *with* activation of their monotonicity filters—see Equations (1.8) and (1.10) in Reference [1] for the definition of PPM's filter. Thus all four schemes (denoted by PSM, PPM, PSM-M and PPM-M) differ only in their reconstruction module.

4.1. Uniform advection of an irregular signal

The initial field $\bar{\rho}(x,0;C_1)$ for uniform advection of an irregular signal is given (as in Reference [12]) by (30), where $C_1 = [10, 0.3, -20, 0.6, 0.3, 11, 0.4, 10, 0.5, 200, 0.1, 0.3, 1]$, and it is advected with uniform velocity $U = 1$ on a uniform grid $\Delta x_i = \Delta x = \text{constant}$, with $N = 50$ intervals, and $L = 1/2$. The timestep $\Delta t = 1/N_t$, where $N_t = 38$ is the number of timesteps per period, and the Courant number $\varepsilon \equiv U\Delta t/\Delta x \simeq 1.3$.

Table IV displays the errors for PSM, PPM, PSM-M and PPM-M for this problem after one and five periods. It can be seen that overall PSM is more accurate than PPM. Furthermore, the present monotonic filter is more selective and damps less than that of PPM. This is evident in Figures 1 and 2 which graphically display the results summarized in

Table IV. Comparison of errors for uniform advection of an irregular signal for 1 and 5 periods with $N_t = 38$ timesteps per period and $\varepsilon \equiv U\Delta t/\Delta x \simeq 1.3$.

	l_1	l_2	l_∞	$l_{\min}$	$l_{\max}$
$p = 1$ (1 period)					
PSM	0.04124	0.06647	0.14795	−0.04899	−0.03574
PPM	0.04987	0.07764	0.17581	−0.07327	−0.02943
PSM-M	0.03728	0.06853	0.14481	0.00000	−0.05400
PPM-M	0.04671	0.07956	0.15723	0.00000	−0.08269
$p = 5$ (5 periods)					
PSM	0.05667	0.08835	0.18713	−0.05069	−0.03932
PPM	0.06544	0.09944	0.20820	−0.07106	−0.04385
PSM-M	0.05370	0.08861	0.18226	0.00002	−0.05044
PPM-M	0.06947	0.10396	0.19312	0.00001	−0.11119

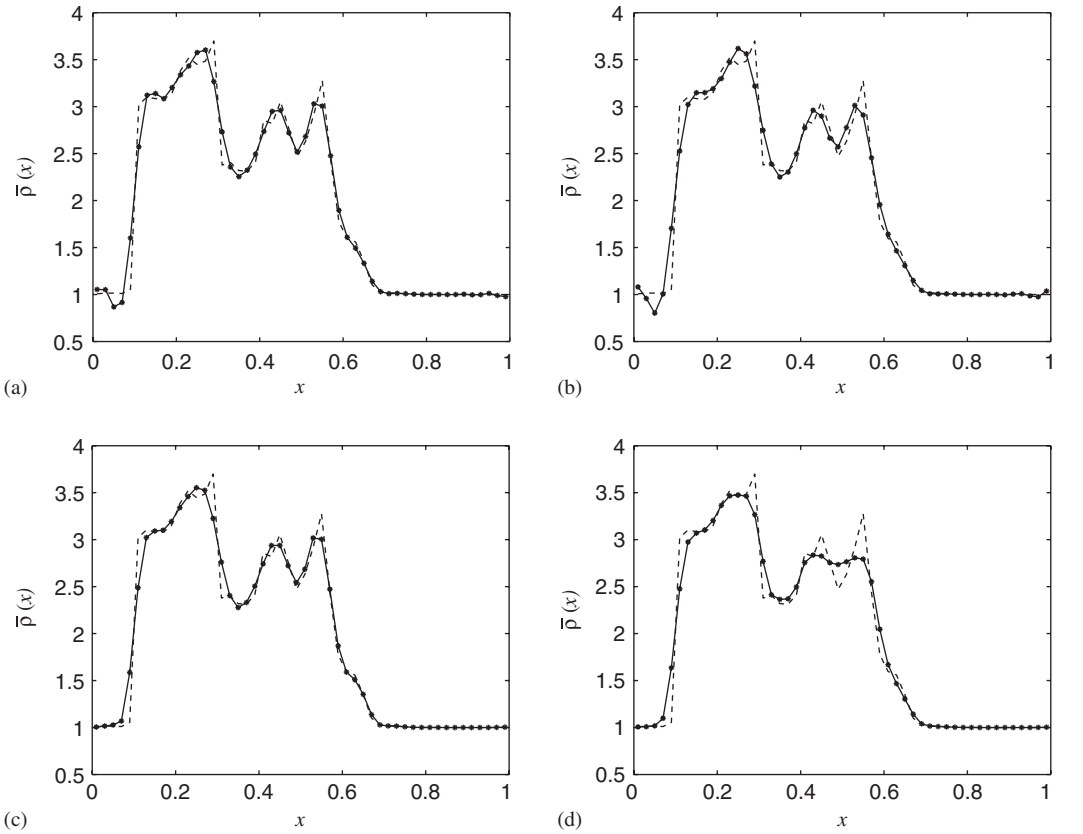

Figure 1. Results after one complete period for the uniform advection of an irregular signal: (a) PSM; (b) PPM; (c) PSM-M; and (d) PPM-M. Parameters as in Table IV, and numerical solutions are shown with asterisks and continuous lines whilst analytical solutions are in dashed lines.

Table IV. After one period (Figure 1), it can be seen that PSM-M selectively removes the undershoot that appears for x a little smaller than $x = 0.1$, and the overshoot for x a little larger, with negligible impact elsewhere. Although PPM-M similarly eliminates the undershoot/overshoot around $x = 0.1$, it has a significant impact elsewhere (spurious damping/smoothing) and, in particular, it spuriously flattens $\bar{\rho}$ in the region $0.4 < x < 0.6$, in a similar manner to that observed in Reference [8] when PPM is used with its monotonic filter. This excessive smoothing by PPM-M is even more pronounced after an integration time of five periods as shown in Figure 2. By contrast, after five periods, PSM-M again maintains consistent results with PSM. The filter is very selective and has minimal effect in the monotonic regions (cf. Figure 2(c) with Figure 2(a)), in contradistinction to the PPM-M solution which is excessively smooth. Summarizing, the present PSM monotonic filter has a similar behaviour to that of PPM near discontinuities. However, results differ significantly around the smooth

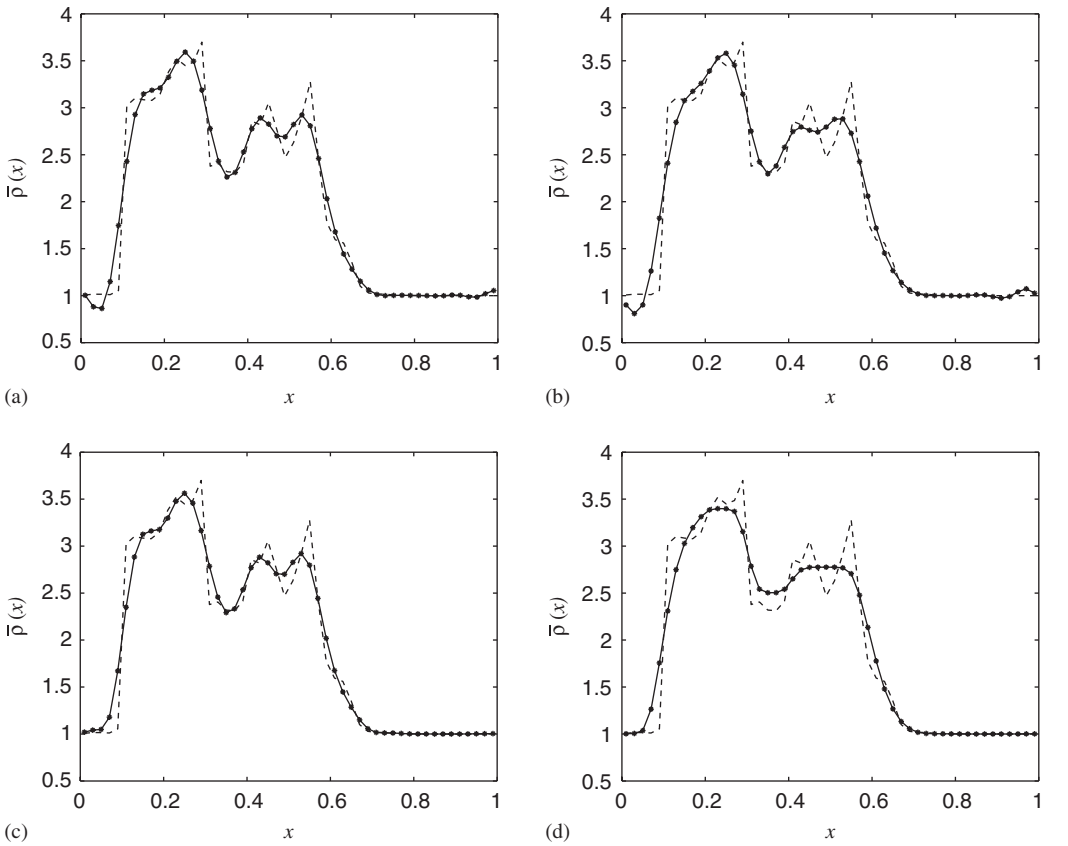

Figure 2. As in Figure 1 but for 5 periods: (a) PSM; (b) PPM; (c) PSM-M; and (d) PPM-M.

part of the solution—the PSM filter is more selective and damps significantly less than that of PPM.

4.2. *Uniform advection of a steep gradient profile*

The initial field $\bar{\rho}(x,0;C_2)$ for uniform advection of a steep gradient profile is given (as in Reference [12]) by (30), where $C_2=[200,0.1,-200,0.7,0,0,0,0,0,100,0.3,0.5,0]$. It is advected using the same parameters as in the previous problem except that $N_t=71$ and $\varepsilon\simeq 0.7$.

Table V displays the errors for PSM, PPM, PSM-M and PPM-M for this problem. Similarly as for the previous problem, PSM is more accurate overall than PPM. Figures 3 and 4 graphically display the results summarized in Table V. Because the profile is a composition of quasi-step functions, there is little risk of excessive damping for the smooth (almost piecewise constant) part of the solution. It is seen that, as is to be expected, both filters behave very similarly (cf. Figure 3(c) with Figure 3(d), and Figure 4(c) with Figure 4(d)).

Table V. Comparison of errors for uniform advection of a steep-gradient profile for 1 and 5 periods with $N_t = 71$ timesteps per period and $\varepsilon \equiv U\Delta t/\Delta x \simeq 0.7$.

	l_1	l_2	l_∞	$l_{\min}$	$l_{\max}$
$p = 1$ (1 period)					
PSM	0.06805	0.09068	0.14953	−0.04434	0.03617
PPM	0.09023	0.10490	0.17220	−0.05094	0.04139
PSM-M	0.05848	0.08961	0.14395	0.00000	−0.00022
PPM-M	0.06301	0.09575	0.15071	0.00000	−0.00007
$p = 5$ (5 periods)					
PSM	0.10491	0.11817	0.17850	−0.03928	0.03354
PPM	0.12144	0.13117	0.19534	−0.04650	0.04666
PSM-M	0.08825	0.11380	0.17285	0.00001	−0.00025
PPM-M	0.09114	0.12099	0.17580	0.00000	−0.00148

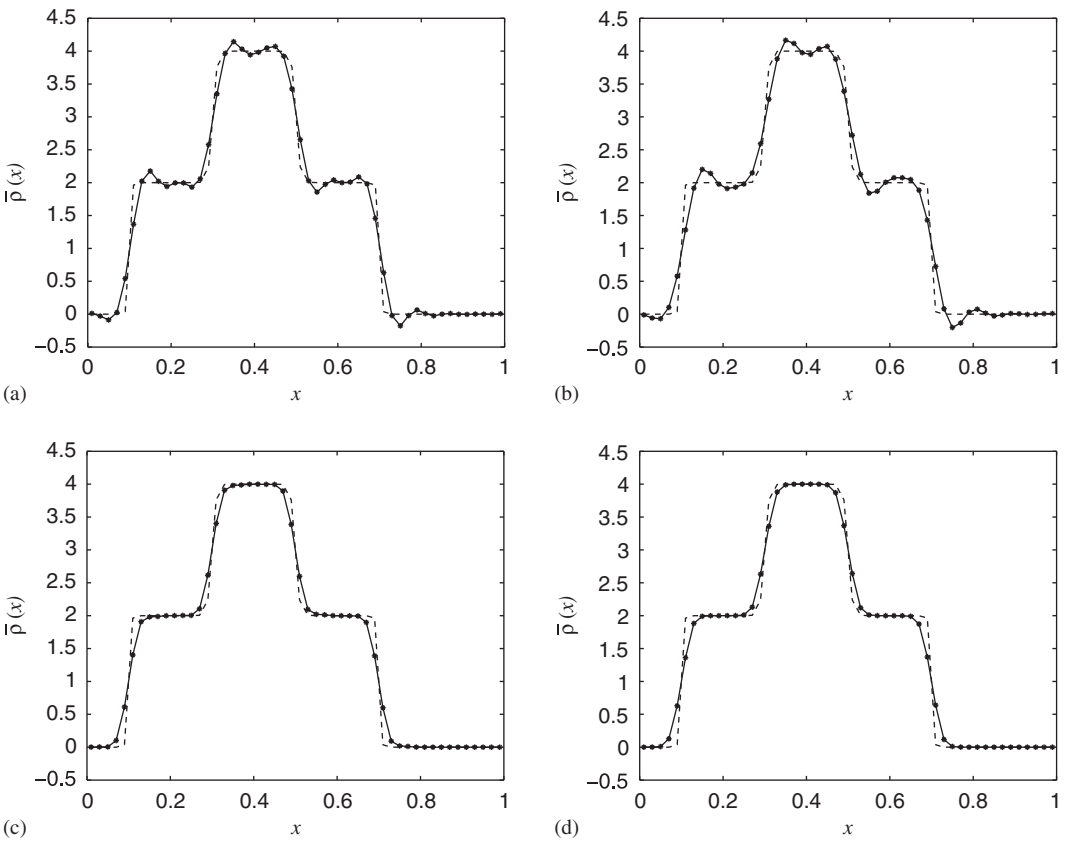

Figure 3. As in Figure 1 but for uniform advection of a steep-gradient profile with $\varepsilon \simeq 0.7$: (a) PSM; (b) PPM; (c) PSM-M; and (d) PPM-M.

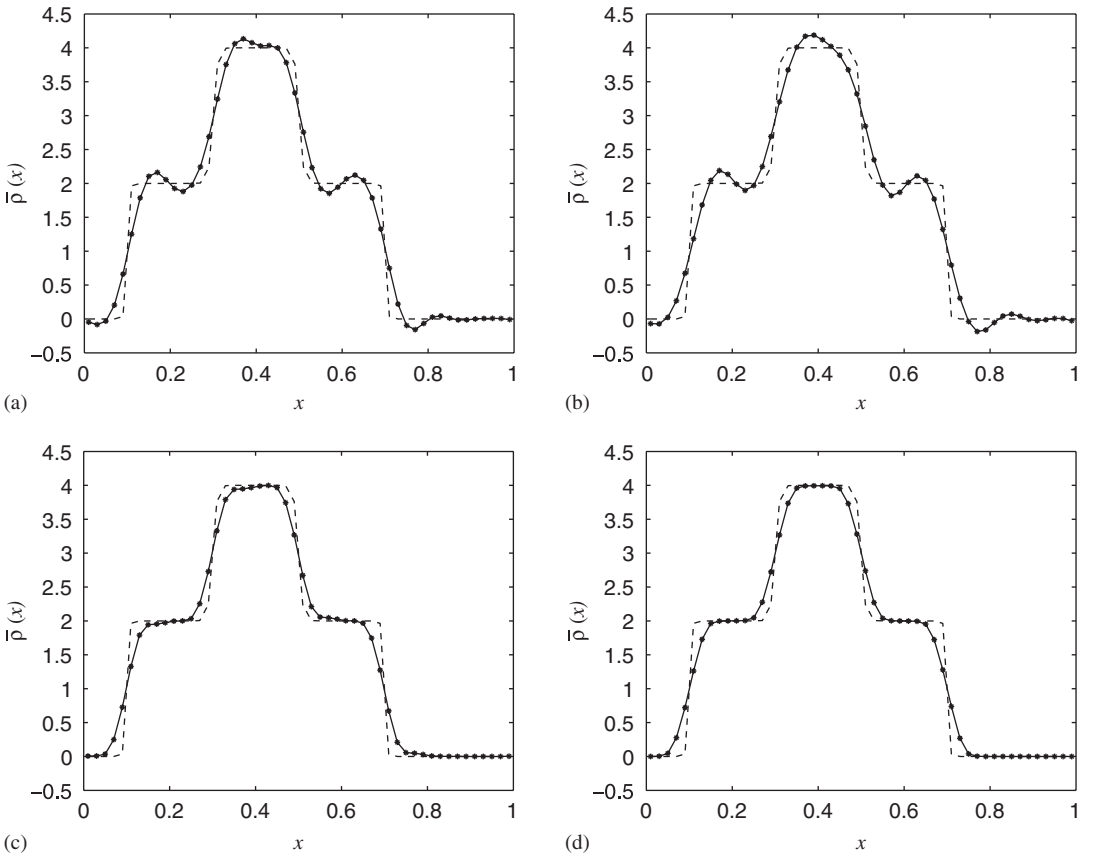

Figure 4. As in Figure 3 but for 5 periods: (a) PSM; (b) PPM; (c) PSM-M; and (d) PPM-M.

5. CONCLUSIONS

A parabolic spline based remapping has been presented and tested for transport problems. Of all piecewise parabolic functions that satisfy the given mass (average density) distribution, it is an optimal reconstruction, since it possesses the *minimum norm* (*or curvature*) and the *best approximation* properties [15].

A monotonicity filter is also incorporated into the proposed scheme. The steepening introduced here improves further the filter presented in Reference [12]. The results show that the present filter is more selective and less damping than that used in the original PPM [1]. Whilst removing spurious under/overshoots near discontinuities, the PSM filter has minimal effect on the smooth part of the solution, unlike the PPM filter.

An operation count shows PSM to be 60% more efficient than PPM whilst a truncation error analysis shows that both have the same order of accuracy. For a uniform grid they in fact have the same asymptotic error. This is confirmed with an idealized infinitely differentiable sine wave on a periodic domain. However, for the more practical case of the advection of

a cosine-squared hill, PSM is found to be significantly more accurate than PPM even in the converged limit. This is due to the slow spectral decay of the shape. Analysis of the problem shows that for the asymptotic truncation error to be applicable to such problems the spectral decay of the shape being advected has to be faster than the order of the truncation error (this was confirmed empirically by advection of the generalized cosine hill). This is of particular interest for atmospheric flows which have slow spectral decay. This also highlights the limitations of convergence tests for practical applications.

For higher dimensional remapping, this 1D-algorithm can be combined with a splitting strategy. This can be a fixed-directional splitting (e.g. the Lin and Rood scheme with PPM [17]) or flow-dependent splitting such as the SLICE approach [2, 3]. This makes possible an accurate remapping for higher-dimensional problems without incurring a prohibitive computational cost, as demonstrated in Reference [19] for the SLICE approach in both Cartesian and spherical geometries.

APPENDIX A: COMPUTATIONAL EFFICIENCY COMPARISON

Consider the PPM and PSM algorithms (i.e. reconstruction and integration without the monotonicity or steepening components) in a 1D context. Consider also a grid that is variable in space and time, as is the case for application of Lagrangian based grids (e.g. Colella and Woodward, [1, p. 175], SLICE [2, 3], and other temporal and spatially adaptive grids [24]). Each algorithm is optimized and an operation count per node (or grid-point) is obtained.

A.1. PPM

The reconstruction part of PPM is (1.6) and (1.7) in Reference [1]. These equations can be rewritten in an optimized form as

$$\rho_{j+1/2} = \bar{\rho}_j + h_j(d_{j+1/2} + m_{j+1/2}) \tag{A1}$$

where

$$m_{j+1/2} = \frac{h_{j+1}}{b_{j-1/2} + b_{j+3/2}}[2d_{j+1/2}(k_j - l_{j+1}) - k_j c_{j+1} + l_{j+1}c_j] \tag{A2}$$

$$c_j = \frac{1}{b_{j-1/2} + h_{j+1}}[(h_{j-1} + b_{j-1/2})d_{j+1/2} + (b_{j+1/2} + h_{j+1})d_{j-1/2}] \tag{A3}$$

$$k_j = \frac{b_{j-1/2}}{f_{j+1/2}}, \quad l_{j+1} = \frac{b_{j+3/2}}{g_{j+1/2}}, \quad f_{j+1/2} = h_j + b_{j+1/2}, g_{j+1/2} = b_{j+1/2} + h_{j+1} \tag{A4}$$

$$b_{j+1/2} = h_j + h_{j+1}, \quad d_{j+1/2} = (\bar{\rho}_{j+1} - \bar{\rho}_j)/b_{j+1/2} \tag{A5}$$

Assuming a Courant number $\varepsilon < 1$, the integration part of the algorithm consists of computing $\bar{\rho}_j^{n+1}$ using (6) and (24), i.e.

$$\bar{\rho}_j^{n+1} \equiv \frac{(M_j^d)^n}{h_j} = \int_{\xi_j}^{1} \rho_j(\xi)\,\mathrm{d}\xi + \frac{h_{j+1}}{h_j}\int_0^{\xi_{j+1}} \rho_{j+1}(\xi)\,\mathrm{d}\xi = (\bar{\rho}_j - M_{j-1}) + \frac{h_{j+1}}{h_j}M_j \tag{A6}$$

where

$$M_j \equiv \int_0^{\xi_{j+1}} \rho_{j+1}(\xi)\,\mathrm{d}\xi = a_{j+1}^{(0)}\xi_{j+1} + a_{j+1}^{(1)}\xi_{j+1}^2/2 + a_{j+1}^{(2)}\xi_{j+1}^3/3$$
$$= \xi_{j+1}[\rho_{j-1/2} - \xi_{j+1}(\rho_{j-1/2} - \bar{\rho}_j + \tilde{a}_{j+1}^{(2)}(1-\xi_{j+1}))] \tag{A7}$$

$$\xi_{j+1} = (x_{j+3/2} - x_{j+1/2}^d)/h_{j+1} \tag{A8}$$

$$\tilde{a}_{j+1}^{(2)} = \rho_{j-1/2} + \rho_{j+1/2} + 2\bar{\rho}_j \tag{A9}$$

From (A1)–(A5) the Number of Operations (NO) for the reconstruction part of PPM is $\mathrm{NO}_{\mathrm{ppm}}^r = 27$ (i.e. 14 Additions (a)+8 Multiplications (m)+5 Divisions (d), or more succinctly $\mathrm{NO}_{\mathrm{ppm}}^r = 14a+8m+5d$), while for the integration part $\mathrm{NO}_{\mathrm{ppm}}^i = 16$ ($=9a+5m+2d$). The total number of arithmetic operations is therefore $\mathrm{NO}_{\mathrm{ppm}} = \mathrm{NO}_{\mathrm{ppm}}^r + \mathrm{NO}_{\mathrm{ppm}}^i = 43$ ($=23a+13m+7d$).

A.2. PSM

For PSM, (14) is normalized by multiplying through by h_i and the resulting equation is solved using the following standard tri-diagonal solver [25]:

$$y_j = h_j/h_{j+1}, \quad r_j = 3(\bar{\rho}_j + y_j\bar{\rho}_{j+1}), \quad u_j = y_j, \quad d_j = 2(1+y_j) \tag{A10}$$

$$t_j = u_{j-1}/c_{j-1}, \quad c_j = d_j - t_j, \quad s_j = r_j - s_{j-1}/c_j, \quad \rho_{j+1/2} = s_j - t_{j+1}\rho_{j+3/2} \tag{A11}$$

The integration part of PSM consists of

$$\bar{\rho}_j^{n+1} = (\bar{\rho}_j - M_{j-1}) + \frac{M_j}{y_j} \tag{A12}$$

together with (A7)–(A9).

For PSM the number of operations for the reconstruction part (A10)–(A11) is $\mathrm{NO}_{\mathrm{psm}}^r = 12$ ($=5a+4m+3d$), while for the integration part (i.e. (A12), (A7), (A8) and (A9)) $\mathrm{NO}_{\mathrm{psm}}^i = 15$ ($=9a+4m+2d$). The total operation count for PSM is $\mathrm{NO}_{\mathrm{psm}} = 27 (= 14a+8m+5d)$. It can be seen that $\mathrm{NO}_{\mathrm{ppm}}/\mathrm{NO}_{\mathrm{psm}} \simeq 1.6$ (i.e. PPM is 60% more expensive than PSM).

APPENDIX B: TRUNCATION ERROR ANALYSIS

In this analysis, a 1D problem with a variable grid and constant wind is considered. Given an average density distribution $\bar{\rho}_i$, $i = 1, 2, \ldots$ the problem is to evaluate, analytically and numerically using PPM and PSM, the average density at a Lagrangian cell (k). For simplicity, let the left boundary of the Lagrangian cell $k, x_{k-1/2}$, be inside the Eulerian cell (i), i.e. $x_{k-1/2} = x_{i-1/2} + \varepsilon_i h_i$ ($0 < \varepsilon_i < 1$), and its right boundary $x_{k+1/2}$ be inside the adjacent Eulerian cell ($i+1$), i.e. $x_{k+1/2} = x_{i+1/2} + \varepsilon_{i+1} h_{i+1}$ ($0 < \varepsilon_{i+1} < 1$). In what follows only the methodology

and the principal results are given. The details of a number of coefficients (μ_j, α_j, ω_j, ζ_j, η_j, θ_j, ϑ_j, λ_j, β_j) are omitted for brevity.

Making use of the definition (17), the average density of the Lagrangian cell $k, \bar{\rho}_k^{\text{ana}}$, can be analytically computed as

$$\bar{\rho}_k^{\text{ana}} \equiv \frac{R(x_{k+1/2}) - R(x_{k-1/2})}{x_{k+1/2} - x_{k-1/2}} \equiv \frac{R(x_{i+1/2} + \varepsilon_{i+1} h_{i+1}) - R(x_{i-1/2} + \varepsilon_i h_i)}{h_i(1 - \varepsilon_i) + \varepsilon_{i+1} h_{i+1}} \tag{B1}$$

The first 6 terms of the Taylor series expansion of $R(y)$ about the centre-point $x_k = (x_{k-1/2} + x_{k+1/2})/2$ in terms of $R(x_k)$ and its derivatives are, for an arbitrary y

$$R(y) = R(x_k) + (y - x_k)\frac{\mathrm{d}R}{\mathrm{d}x}(x_k) + \cdots + \frac{1}{120}(y - x_k)^5 \frac{\mathrm{d}^5 R}{\mathrm{d}x^5}(x_k) + O((y - x_k)^6) \tag{B2}$$

Using (B2), $R(x_{i+1/2} + \varepsilon_{i+1} h_{i+1})$ and $R(x_{i-1/2} + \varepsilon_i h_i)$ can be expanded about x_k and substituted into (B1) to give

$$\bar{\rho}_k^{\text{ana}} = \frac{\mathrm{d}R}{\mathrm{d}x}(x_k) + \mu_3 \frac{\mathrm{d}^3 R}{\mathrm{d}x^3}(x_k) + \mu_5 \frac{\mathrm{d}^5 R}{\mathrm{d}x^5}(x_k) + \cdots \tag{B3}$$

where $\mu_j = \mu_j(h_i, h_{i+1}, \varepsilon_i, \varepsilon_{i+1})$.

B.1. PPM error analysis

Equations (1.6) and (1.7) in Reference [1] are used to evaluate the boundary values $\rho_{j+1/2}$, $j = i-1, i, i+1$ of the piecewise parabolae for the Eulerian cells $(i, i+1)$. These estimates are used to define two adjacent parabola $\rho_i(\xi)$ and $\rho_{i+1}(\xi)$ using (9). Once these parabolae are defined, the average density for the Lagrangian cell (k) of length $h_k \equiv x_{k+1/2} - x_{k-1/2} \equiv h_i(1-\varepsilon_i) + \varepsilon_{i+1} h_{i+1}$, can be computed as

$$\bar{\rho}_k^{\text{ppm}} \equiv \frac{h_i}{h_k} \int_{\varepsilon_i}^{1} \rho_i(\xi)\,\mathrm{d}\xi + \frac{h_{i+1}}{h_k} \int_{0}^{\varepsilon_{i+1}} \rho_{i+1}(\xi)\,\mathrm{d}\xi = \sum_{j=i-2}^{j=i+3} \alpha_j \bar{\rho}_j \tag{B4}$$

where $\alpha_j = \alpha_j(h_{m=i-2,\ldots,i+3}, \varepsilon_i, \varepsilon_{i+1})$. Making use of (17), (B4) can be rewritten in terms of the $R_{j-1/2}$'s as

$$\bar{\rho}_k^{\text{ppm}} = \sum_{j=i-2}^{j=i+4} \alpha_{j-1/2} R_{j-1/2} \tag{B5}$$

where $\alpha_{j-1/2} = \alpha_{j-1/2}(h_{m=i-2,\ldots,i+3}, \varepsilon_i, \varepsilon_{i+1})$. Using (B2), each $R_{j-1/2}$ is expanded about the centre point of the Lagrangian cell, x_k, i.e.

$$R_{j-1/2} = R(x_k) + (x_{j-1/2} - x_k)\frac{\mathrm{d}R}{\mathrm{d}x}(y) + \cdots + \frac{1}{120}(x_{j-1/2} - x_k)^5 \frac{\mathrm{d}^5 R}{\mathrm{d}x^5}(x_k) + O((x_{j-1/2} - x_k)^6) \tag{B6}$$

Substituting (B6) into (B5), it is found that

$$\bar{\rho}_k^{\text{ppm}} = \frac{\mathrm{d}R}{\mathrm{d}x}(x_k) + \mu_3 \frac{\mathrm{d}^3 R}{\mathrm{d}x^3}(x_k) + \omega_4 \frac{\mathrm{d}^4 R}{\mathrm{d}x^4}(x_k) + \omega_5 \frac{\mathrm{d}^5 R}{\mathrm{d}x^5}(x_k) + \cdots \tag{B7}$$

where $\omega_j = \omega_j(h_{m=i-2,\ldots,i+3}, \varepsilon_i, \varepsilon_{i+1})$. The error of the PPM algorithm, E_{ppm}, is therefore

$$E_{\text{ppm}} \equiv \bar{\rho}_k^{\text{ppm}} - \bar{\rho}_k^{\text{ana}} = \gamma_4 \frac{\mathrm{d}^4 R}{\mathrm{d}x^4}(x_k) + \gamma_5 \frac{\mathrm{d}^5 R}{\mathrm{d}x^5}(x_k) + \cdots \tag{B8}$$

where $\gamma_j = \omega_j - \mu_j$, and in particular $\gamma_4 = \omega_4$ and is given by

$$\gamma_4 = \frac{1}{24} \frac{h_i^4 \varepsilon_i^2 (\varepsilon_i - 1)^2 - h_{i+1}^4 \varepsilon_{i+1}^2 (\varepsilon_{i+1} - 1)^2}{h_i(\varepsilon_i - 1) - \varepsilon_{i+1} h_{i+1}} \tag{B9}$$

It can be seen from (B8), that PPM is third-order accurate in space for non-uniform grid. It can also be seen that for a uniform grid and a constant wind (i.e. $h_i = h$ and $\varepsilon_i = \varepsilon$), $\gamma_4 = 0$ and PPM is fourth-order accurate. For a non-uniform grid, γ_5 is a long expression that reduces to $\gamma_5 = \varepsilon^2 h^4 (\varepsilon - 1)^2/24$ for a uniform grid.

B.2. PSM error analysis

For PSM, all the terms in (14) are expanded in terms of Taylor series of the cumulative mass function R and its derivatives about the point $y \equiv x_{i+1/2}$. This results in

$$\rho_{i+1/2} = \frac{\mathrm{d}R}{\mathrm{d}x}(y) + \frac{1}{72}(h_i^2 h_{i+1} - h_{i+1}^2 h_i) \frac{\mathrm{d}^4 R}{\mathrm{d}x^4}(y) + \frac{1}{180}(h_i^2 h_{i+1}^2 - h_i h_{i+1}^3 - h_{i+1} h_i^3) \frac{\mathrm{d}^5 R}{\mathrm{d}x^5}(y) + \cdots \tag{B10}$$

Using (B10) (and similar equations for $\rho_{i-1/2}$ and $\rho_{i+3/2}$), the two adjacent parabolae $\rho_i(\xi)$ and $\rho_{i+1}(\xi)$ are defined. Then the integral (B4) is evaluated in terms of $R(x_{i+1/2})$ and its derivatives. This can be expressed as

$$\bar{\rho}_k^{\text{psm}} = \sum_{j=i}^{i+2} \zeta_j R(x_{j-1/2}) + \sum_{j=1} \eta_j \frac{\mathrm{d}^j R}{\mathrm{d}x^j}(x_{i-1/2}) + \sum_{j=1} \theta_j \frac{\mathrm{d}^j R}{\mathrm{d}x^j}(x_{i+1/2}) + \sum_{j=1} \vartheta_j \frac{\mathrm{d}^j R}{\mathrm{d}x^j}(x_{i+3/2}) \tag{B11}$$

where $\zeta_j = \zeta_j(h_{m=i-2,\ldots,i+3}, \varepsilon_i, \varepsilon_{i+1})$, $\eta_j = \eta_j(h_{m=i-2,\ldots,i+3}, \varepsilon_i, \varepsilon_{i+1})$, $\theta_j = \theta_j(h_{m=i-2,\ldots,i+3}, \varepsilon_i, \varepsilon_{i+1})$, and $\vartheta_j = \vartheta_j(h_{m=i-2,\ldots,i+3}, \varepsilon_i, \varepsilon_{i+1})$. Using the Taylor series (B2), all the $R(x_{j-1/2})$ and $\mathrm{d}^j R/\mathrm{d}x^j$ in (B11) are expressed in terms of $R(x_k)$ and its derivatives, and then substituted back into (B11). This gives

$$\bar{\rho}_k^{\text{psm}} = \frac{\mathrm{d}R}{\mathrm{d}x}(x_k) + \mu_3 \frac{\mathrm{d}^3 R}{\mathrm{d}x^3}(x_k) + \lambda_4 \frac{\mathrm{d}^4 R}{\mathrm{d}x^4}(x_k) + \lambda_5 \frac{\mathrm{d}^5 R}{\mathrm{d}x^5}(x_k) + \cdots \tag{B12}$$

where $\lambda_j = \lambda_j(h_{m=i-2,\ldots,i+3}, \varepsilon_i, \varepsilon_{i+1})$. Finally, the error due to PSM can be expressed as

$$E_{\text{psm}} = \beta_4 \frac{\mathrm{d}^4 R}{\mathrm{d}x^4}(x_k) + \beta_5 \frac{\mathrm{d}^5 R}{\mathrm{d}x^5}(x_k) + \cdots \tag{B13}$$

where $\beta_j = \lambda_j - \mu_j$. In particular $\beta_4 = \lambda_4$ is given by

$$\begin{aligned} \beta_4 = \{ & h_{i+1}^2 h_{i+2} \varepsilon_{i+1}^2 (\varepsilon_{i+1} - 1)(h_{i+1} - h_{i+2}) + h_i^2 h_{i+1} \varepsilon_i^2 (\varepsilon_i - 1)(h_{i+1} - h_i) \\ & + h_i^2 h_{i-1} \varepsilon_i (\varepsilon_i - 1)^2 (h_i - h_{i-1}) + h_{i+1}^2 h_i \varepsilon_{i+1} (\varepsilon_{i+1} - 1)^2 (h_i - h_{i+1}) \\ & + 3 h_i^4 \varepsilon_i^2 (\varepsilon_i - 1)^2 - 3 h_{i+1}^4 \varepsilon_{i+1}^2 (\varepsilon_{i+1} - 1)^2 \} / 72 (h_i(\varepsilon_i - 1) - \varepsilon_{i+1} h_{i+1}) \end{aligned} \tag{B14}$$

Similarly as for PPM, PSM is third-order accurate in space for a non-uniform grid, and fourth-order accurate for a uniform grid and constant wind (i.e. $\beta_4 = 0$ for $h_i = h$ and $\varepsilon_i = \varepsilon$). For a non-uniform grid β_5 is a long expression that reduces to $\beta_5 = \varepsilon^2 h^4(\varepsilon - 1)^2/24$ (i.e. $\beta_5 = \gamma_5$) for a uniform grid.

APPENDIX C: ERROR MEASURES

Performance is measured using the error measures suggested by Williamson *et al*. [20], viz.

$$l_1 \equiv \frac{I(|\bar{\rho}^{\text{num}} - \bar{\rho}^{\text{an}}|)}{I(|\bar{\rho}^{\text{an}}|)} \tag{C1}$$

$$l_2 \equiv \frac{\sqrt{I(([\bar{\rho}^{\text{num}} - \bar{\rho}^{\text{an}}])^2)}}{\sqrt{I([\bar{\rho}^{\text{an}}]^2)}} \tag{C2}$$

$$l_\infty \equiv \frac{\max(|\bar{\rho}^{\text{num}} - \bar{\rho}^{\text{an}}|)}{\max(|\bar{\rho}^{\text{an}}|)} \tag{C3}$$

$$l_{\min} \equiv \frac{\min(\bar{\rho}^{\text{num}}) - \min(\bar{\rho}^{\text{an}})}{\max(\bar{\rho}^{\text{an}}) - \min(\bar{\rho}^{\text{an}})} \tag{C4}$$

$$l_{\max} \equiv \frac{\max(\bar{\rho}^{\text{num}}) - \max(\bar{\rho}^{\text{an}})}{\max(\bar{\rho}^{\text{an}}) - \min(\bar{\rho}^{\text{an}})} \tag{C5}$$

where $\bar{\rho}^{\text{num}}$ and $\bar{\rho}^{\text{an}}$ refer to the numerical and analytical solutions, respectively, and $I(\bar{\rho})$ is a global integral (or global mass) given by

$$I(\bar{\rho}) \equiv \sum_{i=1}^{N} \bar{\rho}_i h_i \cong \int_0^{2L} \rho(x,t)\,\mathrm{d}x \tag{C6}$$

ACKNOWLEDGEMENTS

The authors gratefully acknowledge the help provided by the editor and the two referees.

REFERENCES

1. Colella P, Woodward P. The piecewise parabolic method (PPM) for gas-dynamical simulations. *Journal of Computational Physics* 1984; **54**:174–201.
2. Zerroukat M, Wood N, Staniforth A. SLICE: a semi-Lagrangian inherently conserving and efficient scheme for transport problems. *Quarterly Journal of the Royal Meteorological Society* 2002; **128**:2801–2820.
3. Zerroukat M, Wood N, Staniforth A. SLICE-S: a semi-Lagrangian inherently conserving and efficient scheme for transport problems on the sphere. *Quarterly Journal of the Royal Meteorological Society* 2004; **130**:2649–2664.
4. Rančić M. An efficient conservative monotonic remapping for semi-Lagrangian transport algorithms. *Monthly Weather Review* 1995; **123**:1213–1217.
5. Laprise J, Plante A. A class of semi-Lagrangian integrated mass (SLIM) numerical transport algorithms. *Monthly Weather Review* 1995; **123**:553–565.
6. Machenhauer B, Olk M. On the development of a cell-integrated semi-Lagrangian shallow water model on the sphere. *ECMWF Workshop Proceedings*: *Semi-Lagrangian Methods*. ECMWF: Reading, U.K., 1996; 213–228.

7. Machenhauer B, Olk M. The implementation of the semi-implicit cell-integrated semi-Lagrangian models. *Atmosphere-Ocean* 1997; **35**:103–126 (special issue).
8. Xiao F, Yabe T. Completely conservative and oscillationless semi-Lagrangian schemes for advection transportation. *Journal of Computational Physics* 2001; **170**:498–522.
9. Nair R, Machenhauer B. The mass conservative cell-integrated semi-Lagrangian advection scheme on the sphere. *Monthly Weather Review* 2002; **130**:649–667.
10. Nair R, Scroggs J, Semazzi F. Efficient conservative global transport schemes for climate and atmospheric chemistry models. *Monthly Weather Review* 2002; **130**:2059–2073.
11. Nair R, Scroggs J, Semazzi F. A forward trajectory global semi-Lagrangian transport scheme. *Journal of Computational Physics* 2003; **190**:275–294.
12. Zerroukat M, Wood N, Staniforth A. A monotonic and positive-definite filter for a semi-Lagrangian inherently conserving and efficient (SLICE) scheme. *Quarterly Journal of the Royal Meteorological Society* 2005; **131**:2923–2936.
13. Staniforth A, Côté J. Semi-Lagrangian integration schemes for atmospheric models—a review. *Monthly Weather Review* 1991; **119**:2206–2223.
14. van Leer B. Towards the ultimate conservative difference scheme IV: a new approach to numerical convection. *Journal of Computational Physics* 1977; **23**:276–299.
15. Ahlberg JH, Nilson EN, Walsh JL. *The Theory of Splines and Their Applications* (1st edn). Academic Press: London, 1967.
16. Press W, Teukolsky S, Vetterling W, Flannery B. *Numerical Recipes in Fortran 77*. Cambridge University Press: Cambridge, U.K., 1992.
17. Lin SJ, Rood RB. Multidimensional flux-form semi-Lagrangian transport schemes. *Monthly Weather Review* 1996; **124**:2046–2070.
18. Strang G. On the construction and comparison of difference schemes. *SIAM Journal on Numerical Analysis* 1968; **5**:506–517.
19. Zerroukat M, Wood N, Staniforth A. Application of the parabolic spline method (PSM) to a multi-dimensional conservative transport scheme (SLICE). *International Journal for Numerical Methods in Fluids*, submitted.
20. Williamson DL, Drake JB, Hack JJ, Jakob R, Swarztrauber PN. A standard test set for numerical approximations to the shallow-water equations in spherical geometry. *Journal of Computational Physics* 1992; **102**:221–224.
21. Nastrom GD, Gage KS. A climatology of atmospheric wavenumber spectra of wind and temperature observed by commercial aircraft. *Journal of the Atmospheric Sciences* 1985; **42**:950–960.
22. Tung KK, Orlando WW. The k^{-3} and $k^{-5/3}$ energy spectrum of atmospheric turbulence: quasigeostrophic two-level model simulation. *Journal of the Atmospheric Sciences* 2003; **60**:824–835.
23. Panofsky HA, Dutton JA. *Atmospheric Turbulence*. Wiley: London, 1984.
24. Thompson JF. A survey of dynamically-adaptive grids in the numerical solution of partial-differential equations. *Applied Numerical Mathematics* 1985; **1**:3–27.
25. Golub GH, van Loan CF. *Matrix Computations* (3rd edn). Johns Hopkins University Press: Baltimore, MD, U.S.A., 1996.

